Appl. Phys. A 87, 569–575 (2007)
DOI: 10.1007/s00339-007-3903-2

Applied Physics A
Materials Science & Processing

G. MÉSZÁROS[1,*]
S. KRONHOLZ[2]
S. KARTHÄUSER[2]
D. MAYER[1]
T. WANDLOWSKI[1,✉]

Electrochemical fabrication and characterization of nanocontacts and nm-sized gaps

[1] Institute of Bio- and Nanosystems IBN, Research Center Jülich GmbH, 52425 Jülich, Germany
[2] Institute of Solid State Physics and CNI – Center of Nanoelectronic Systems for Information Technology, Research Center Jülich GmbH, 52425 Jülich, Germany

Received: 7 September 2006/Accepted: 11 December 2006
Published online: 9 March 2007 •

ABSTRACT Copper nanocontacts and molecular-sized nanogaps were prepared and characterized at electrified solid/liquid interfaces employing lithographic and electrochemical techniques. A dedicated four-electrode potentiostat was developed for controlling the electrochemical fabrication process and for monitoring the electrical characteristics of the nanostructures created. The formation and breaking of Cu nanocontacts exhibits conductance quantization characteristics. The statistical analysis of conductance histograms revealed a preferential stability of nanocontacts with integer values of G_0, with a clear preference for 1 G_0, 2 G_0 and 3 G_0. The growth of molecular-sized gaps shows quantized tunneling current, which is attributed to the discrete nature of Cu atoms, water molecules, and specifically adsorbed ions.

PACS 73.23Ad; 73.63.Rt; 82.45.Yz; 85.35.-p

1 Introduction

As the miniaturization of electronic components approaches the nanometer scale new concepts to tailor structure, functionality and fabrication strategies are essential [1]. The bottom up assembly of well-defined nanoscale building blocks, such as tailored molecules [2, 3], nanocrystals [4], quantum dots [5], and nanowires [6–8] having key properties controlled by size, morphology and chemical composition represents an important topic in both fundamental and technology relevant research. Studies of nanostructured materials and devices offer opportunities to explore novel physical, chemical, electrical and electrochemical phenomena and processes at the nanometer scale. One of the major challenges in producing nanoscale electronic devices is the reliable fabrication of nanometer-sized metal electrodes that enable electrical contact to individual chemical nanostructures [9]. Different approaches have been developed to fabricate electrode pairs with molecular scale gaps and metal nanocontacts, such as two-step electron beam lithography [10, 11], nanopore- and template-based methods [12, 13], mechanical break junctions [14–16], electromigration [17] and electrodeposition or dissolution [18–32]. Strategies based on electrochemical concepts involve local probe techniques [18, 20] or supported electrodes on solid substrates, which enable tailoring the composition, shapes and dimensions of the respective nanostructures [18–30, 32]. A variety of metal contacts have been produced including Au [19, 25, 27, 29, 31], Cu [18, 20, 23, 24], Ag [21, 24, 30], Ni [24, 28], Pt [22] and Co[26]. Electrochemically fabricated nanocontacts possess unique electrical, mechanical, magnetic and (electro-) chemical properties at room temperature that are different from their bulk samples [33, 34]. Examples are conductance quantization and conductance changes due to adsorption, high mechanical stability and ballistic magneto resistance behavior [18–20, 28].

Electrochemical techniques were also used to prepare electrode pairs separated with gap distances ranging from less than 1 nm [20, 32] to more than 10 nm [31] for different systems. The precise monitoring and control of the gap width is achieved with dedicated feedback systems. Such signals include the tunneling or ballistic transport current [20], the dc-resistance [20], the ac-impedance [19, 25, 26, 32] or the potential drop in the electrochemical double layer [31] between two facing electrodes. A unique advantage of these electrochemical fabrication methods is the reversibility, e.g. nanostructures can be tuned by electrodeposition and dissolution until the most desirable structure is created. Simultaneously, the electron transport properties are monitored. Advancing these developments further offers new opportunities for exploring quantum phenomena in physical, chemical and electrical processes at room temperature and in an electrochemical environment. One of the most prosperous applications of electrochemically fabricated metal electrodes with nm-sized gaps are fundamental studies on electron transport properties of various (individual) nanostructures, such as tailored clusters, carbon nanotubes, polymer and even molecular or biomolecular junctions [11, 35]. The approach represents a unique concept for interfacing the macroscopic to the nanoworld.

In the present paper we report on the development of a custom-designed low current bipotentiostat for the electrochemical fabrication and characterization of nanocontacts and

✉ Fax: +49 2461 61 3907, E-mail: th.wandlowski@fz-juelich.de
*_Home address_: Institute of Materials and Environmental Chemistry, Chemical Research Centre of the Hungarian Academy of Sciences, Pusztaszeri ut 59–67, 1025 Budapest, Hungary

molecular-sized gaps. Selected applications will be described for the deposition and dissolution of copper nanostructures.

2 Experimental

2.1 *Chip design*

Template chips with 15 pairs of nanoelectrodes as working electrodes (triangular shape with a typical length of 500 nm) and two microelectrodes for calibration purposes (rectangular shape $50 \times 150\,\mu m$) were fabricated employing electron beam and optical lithography in combination with standard lift off techniques. The substrate was covered with a thermally grown silicon oxide layer of 400 nm thickness. The electrodes and leads were prepared by sequential e-beam evaporation of Ti (2 nm), Pt (5 nm) and Au (50 nm) ontop, deposition rate $< 0.05\,nm\,s^{-1}$. The initial separation of the nanoelectrodes varied between 20 nm and 60 nm. All electrodes were interfaced via gold leads to macroscopic contact pads of 1×1 mm. The entire chip was protected with a two-layer coating of hard baked PMMA, except the calibration pads and the access windows of approximately 700×700 nm around each pair of nanoelectrodes. The electrically insulating cover minimizes the electrolyte exposure of the leads, particularly those connecting the nanoelectrodes. Their electrochemical leakage current in the double layer region is typically $\ll 10$ pA. The chip assembly is completed by a glass ring, which was attached via the silicon encapsulant 96-082 (Dow Corning) to the PMMA protection layer. Figure 1a and b illustrate the chip layout and a pair of nanoelectrodes with protection layer. For technical details on the lithographic and deposition routines we refer to our previous publication [36].

2.2 *Electrochemical measurements*

Before each experiment the chip assembly was rinsed with ultrapure Milli-Q water (18 MΩ, TOC $\leq$ 3 ppb). The inner ring compartment was exposed to isopropanol (p.a. KMF). Subsequently, the chip was dried in a stream of 5N argon, and the glass cell was filled with electrolyte. The preassembled cell was then exposed to an ultrasound bath in several short intervals of 5 s to guarantee the complete contact between the nanoelectrodes and the electrolyte, and to remove possible air bubbles from side walls of the access window. After an additional electrolyte exchange the assembly was mounted on the sample stage of a Süss Probe Station 355 PM-V1.

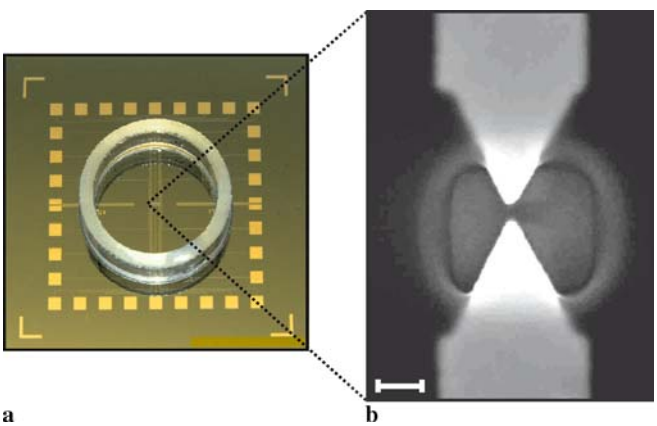

a **b**

FIGURE 1 (**a**) Photograph of the chip assembly with glass ring; (**b**) scanning electron micrograph of a pair of gold electrodes with access window, the scale bar is 200 nm in length

The electrolyte solutions were prepared from Milli-Q water, H_2SO_4 (Merck suprapure) and $CuSO_4$ (Merck, pro analysis). The glassware was cleaned in caroic acid followed by extended rinsing with Milli-Q water.

The electrochemical measurements were carried out either in 0.1 M H_2SO_4 or in 0.1 M H_2SO_4 + 1 mM $CuSO_4$ employing a three-electrode (for the separate characterization of each working electrode WE1 and WE2) or a four-electrode (two working electrodes, WE1 and WE2, in conductance and tunneling experiments) configuration. Flame annealed gold and platinum wires served as counter (CE) and reference (RE) electrodes in bare sulphuric acid. Two copper wires were chosen in copper containing electrolytes. All electrodes were connected to micromanipulators ensuring the electrical contact between the chip assembly and the potentiostat (see Sect. 2.3). The potentials in this paper refer to a Cu|1 mM Cu^{2+} reference in 0.1 M H_2SO_4.

2.3 *Instrumentation*

A low current four-electrode bipotentiostat and custom-made software were developed to control the electrochemical fabrication process and to monitor the electrical characteristics of the created nanostructures. The technical description of the complete set-up will be given in a forthcoming publication [37]. Here we will only focus on some essential characteristics.

The current input stages of the bipotentiostat consist of two temperature-stabilized logarithmic current-to-voltage converters with a maximum resolution of approximately 5 fA (with 0.8 s integration time) and a time constant of ~ 2 ms in the low pA range. Applying a 20th order Fourier series we could compensate the deviation from the ideal logarithmic behavior resulting in an accuracy of about 2% in the 20 pA to 2 mA current range. In the range below 20 pA the linearity is still within 2%, however a very slow drifting with a maximum current offset of ± 0.1 pA arises. All signals are digitized by a 16 bit AD converter while the controlling signals are supplied by 16 bit DA converters. The data acquisition rate and the integration time are user defined (range 0.1 to 800 ms). All timing and data collection tasks are performed by a 8 bit microcontroller that connects to a PC via a galvanically isolated USB interface. The bipotentiostat offers two separate user-defined, digitally generated signals as the potential of the working electrode 1 (E_{WE1}) and as the potential difference between the two working electrodes ($E_{WE2}-E_{WE1}$). A separate analog sweep generator operates in the range between $1\,mV\,s^{-1}$ and $10\,V\,s^{-1}$. An option for modulating the dc voltage with an ac signal of variable frequency (0 to 2 kHz) and amplitude, 180° phase shift between the two working electrodes, was included. This specific mode allows the in-situ electrochemical annealing of the electrodeposited materials on both electrodes while maintaining a small but constant potential difference between WE1 and WE2 for monitoring the conductance characteristics of the junction.

The bipotentiostat and the probe station were placed in a carefully grounded Faraday cage.

3 Results and discussion

3.1 *Electrochemical characterization*

The calibration pads and the nanoelectrodes exposed to the electrolyte were first electrochemically annealed in 0.1 M H_2SO_4 by cycling the potential in the double layer region with 50 mV s^{-1} for 30 min [38]. This treatment produces compact and rather smooth gold thin film electrodes with a roughness factor of 1.6 ± 0.2, e.g. the electrochemical active surface is approximately 1.6 times larger than the projected nominal geometry. Figure 2a shows the typical voltammetric response of freshly prepared calibration pads (nominal size $50 \times 150\,\mu m$) in 0.1 M $H_2SO_4 + 1$ mM $CuSO_4$. Four potential regions labelled I to IV and separated by characteristic current peaks can be distinguished. The voltammetric profile of the microelectrodes resembles those of a gold surface with preferentially (111) oriented terrace sites [39]. The experiment started in the double layer region I at $E = 0.600$ V (vs. $Cu|Cu^{2+}$). Excursion to negative potentials leads to the 2D underpotential deposition of copper (UPD, region II) as indicated by the two pairs of current peaks P1/P1′ and P2/P2′, which represent energetically different adsorption/desorption processes. In the first step (P1/P1′) the transition between randomly adsorbed copper and (hydrogen-) sulfate ions and an ordered $(\sqrt{3} \times \sqrt{3})$ R30° sulphate adlayer co-adsorbed in a honeycomb copper network takes place. The pair of peaks P2/P2′ characterizes the transition of this $(\sqrt{3} \times \sqrt{3})$ R30° phase into a pseudomorphic Cu(1 × 1) monolayer. The 3D bulk or overpotential deposition (OPD) of Cu starts at $E < 0.00$ V (region III) according to an activated Stranski–Krastanov mechanism [39]. The amount of bulk deposited copper increases with more negative deposition potential and longer deposition time. Figure 2a illustrates this trend for a series of negative return potentials E_{Tn} in region III. The heights and the corresponding charges of the dissolution (or stripping) peaks P3′ of bulk deposited Cu increase with E_{Tn} being more negative. The 3D Cu bulk deposits can be completely dissolved at $E > 0.00$ V without major modification of the gold substrate due to surface alloying or dealloying if the residence time in the OPD region III is short, e.g. < 2 min. At $E > 0.00$ V the 2D Cu UPD adlayer is formed again. After an extended potential region of ideal polarizability, the oxidation of the gold surface starts at $E > 1.00$ V (region IV), and a characteristic current peak P4′ evolves at $E = 1.28$ V, which is attributed to the oxidation of (111) terrace sites. P4 represents the corresponding reduction of the surface oxide. The charge consumed is estimated to $Q_{redF} = (960 \pm 200)\,\mu Ccm^{-2}$. Comparing this value to data obtained from the reduction charge of a massive Au(poly) electrode prepared by electrochemical annealing in 0.1 M H_2SO_4 ($Q_{redC} \approx 600\,\mu Ccm^{-2}$) [40], one obtains the roughness factor (1.6 ± 0.3), which was already mentioned above.

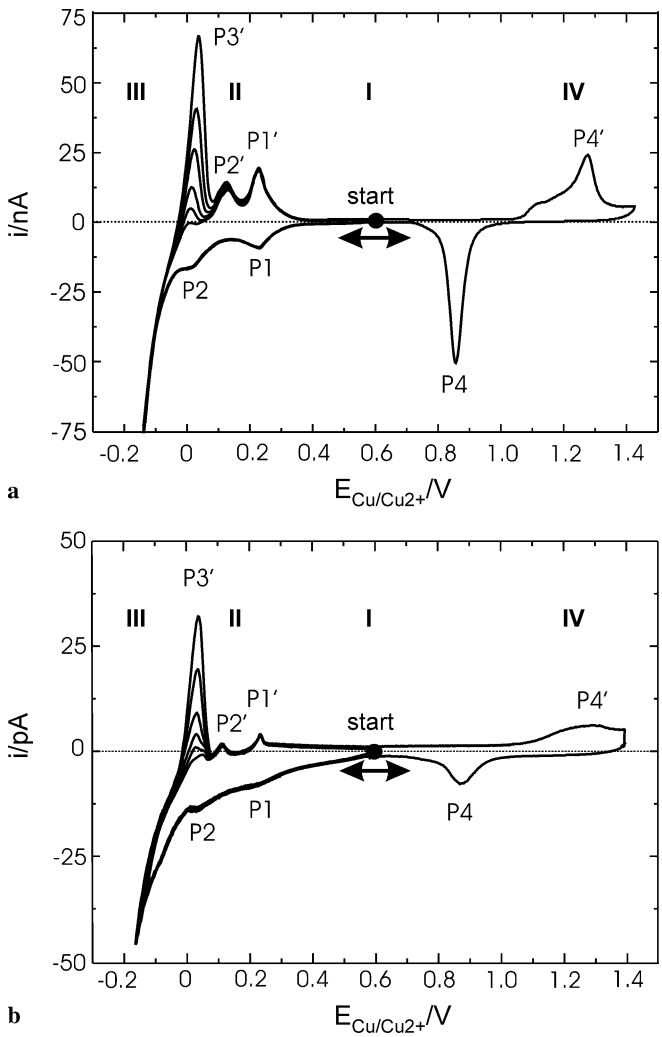

FIGURE 2 Cyclic voltammograms for annealed gold electrodes in 0.1 M $H_2SO_4 + 1$ mM $CuSO_4$, scan rate 50 mV s^{-1}. The potential scans in the positive and negative directions started after equilibration at 0.600 V. Four potential regions labelled I to IV and separated by characteristic current peaks P1/P1′, P2/P2′, P3′ and P4/P4′ can be distinguished. (**a**) Calibration pad ($50 \times 150\,\mu m$). The negative return potentials in the Cu OPD region were −0.110 V, −0.120 V, −0.130 V, −0.140 V, −0.150 V and −0.160 V. (**b**) Nanoelectrode. The negative return potentials in the Cu OPD region were −0.120 V, −0.130 V, −0.140 V, −0.150 V, −0.160 V and −0.170 V

We notice that qualitative identical current vs. voltage characteristics were obtained in 0.1 M $H_2SO_4 + 1$ mM $CuSO_4$ for the just described microelectrodes (Fig. 2a), which serve as calibration pads, as well as for the gold nanoelectrodes (Fig. 2b). The measured currents of the latter are approximately three orders of magnitude smaller, but scale with the electrode area. This result ensures the integrity of the electrode assembly in the access window (cf. Fig. 1b). Comparing the reduction charges of the gold surface oxide for the data plotted in Fig. 2a and b leads to an electrochemically active area of 1.04 μm^2 for the nanoelectrode shown. Considering the estimated roughness factor of 1.6 one obtains for the electrolyte an exposed geometric area 0.65 μm^2. This value is of the same order of magnitude but slightly larger than the suggested free area based on the chip fabrication parameters (cf. Sect. 2.1 and Fig. 1b). The difference is most probably related to the electron beam damage of the PMMA layer at the edges of the protection window, which may cause an additional contact area between electrolyte and gold electrode due to creeping.

3.2 *Formation and dissolution of* Cu *quantum wires*

The formation of Cu nanocontacts was achieved by depositing Cu on one electrode (WE1) only of each pair of pre-fabricated nanoelectrodes (WE1, WE2). The potential of the other electrode WE2 was typically held at values slightly negative of the (1×1) Cu UPD phase (region II), which ensures a negligible low Cu deposition rate. The nucleation of Cu clusters on WE1 was initialized by stepping the electrode potential from the UPD region II to $E_{\mathrm{WE1}} = -0.250\,\mathrm{V}$ in the OPD region III. After a short voltage pulse of 20 ms, sufficient to form critical nuclei, the electrode potential was adjusted at more positive values, but still in region III ensuring a rather slow growth of the 3D Cu bulk phase. The compactness and stability of the Cu deposit were improved in selected experiments by modulating the dc potentials of WE1 and WE2 with a phase adjusted 2 kHz square wave of 0.200 V amplitude. The particular example plotted in Fig. 3a was recorded for $E_{\mathrm{WE1}} = -0.163\,\mathrm{V}$ and $E_{\mathrm{WE2}} = -0.050\,\mathrm{V}$. Four phases of electrodeposition corresponding to different ranges of the electrode separation can be identified from the entire evolution of the monitor current:

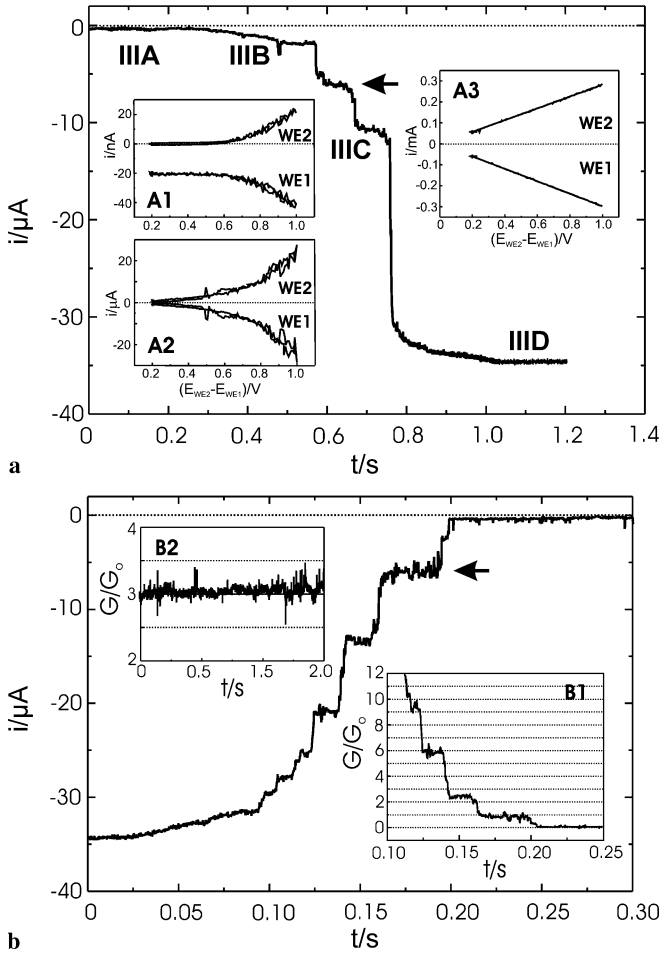

FIGURE 3 Current–time traces of formation (**a**) and dissolution or "etching" (**b**) of a Cu quantum wire fabricated on a pair of gold template electrodes in 0.1 M $H_2SO_4 + 1$ mM $CuSO_4$. Four phases of electrodeposition/dissolution, which are labelled IIIA to IIID, can be distinguished. (**a**) The Cu OPD deposition was initialized by stepping the potential of E_{WE1} to −0.250 V (20 ms). The subsequent growth was monitored for $E_{\mathrm{WE1}} = -0.163\,\mathrm{V}$ and $E_{\mathrm{WE2}} = -0.050\,\mathrm{V}$. The *insets* A1 and A2 represent the current–time responses at various stages of deposition in phase IIIB (tunneling regime) upon sweeping the bias voltage ($E_{\mathrm{WE2}} - E_{\mathrm{WE1}}$) at fixed deposition potential $E_{\mathrm{WE1}} = -0.163\,\mathrm{V}$ with $20\,\mathrm{V\,s^{-1}}$. A3 was recorded in phase IIID under otherwise identical conditions. (**b**) Dissolution of a Cu nanowire upon stepping the potentials $E_{\mathrm{WE1}} = -0.163\,\mathrm{V}$ and $E_{\mathrm{WE2}} = -0.050\,\mathrm{V}$ to $E_{\mathrm{WE1}} = -0.042\,\mathrm{V}$ and $E_{\mathrm{WE2}} = 0.071\,\mathrm{V}$. The *inset* B1 illustrates the normalized conductance trace with characteristic integer conductance steps. B2 is an example of a quantum wire stabilized at 3 G_0

In the first phase IIIA, the dc current at WE1 is rather constant and typically < 100 pA being determined by the diffusion controlled deposition of Cu onto the electrolyte exposed surface of WE1 (Faraday current). The current at WE2 is two to three orders of magnitude smaller.

The second phase IIIB is characterized by an exponential increase of the current up to several hundred nA, which is attributed to direct tunneling between the two working electrodes [19, 20]. The proof for direct tunneling was obtained by performing the following experiment: the potential of WE1 was kept constant at $E_{\mathrm{WE1}} = -0.163\,\mathrm{V}$, e.g. in the Cu OPD region III, while the potential of WE2 was scanned from −0.050 V to 0.85 V with $20\,\mathrm{V\,s^{-1}}$. This approach allows the applying of a large potential difference between the two nanoelectrodes for a short time without modifying the Cu deposition on WE1. One complete cycle requires only 90 ms. The linear offset current at WE1 is caused by the Cu OPD deposition at −0.163 V. The electrochemical current at WE2 is expected to scale linearly with the scan rate due to double layer charging and the surface confined Cu UPD adlayer [41] with an upper limit of approximately 4 nA for $20\,\mathrm{V\,s^{-1}}$. For comparison, we refer to the nanoelectrode voltammogram displayed in Fig. 2b. However, the currents observed are (1) larger, (2) independent on the rate of the voltage scans in $0.10\,\mathrm{V\,s^{-1}} < v < 10\,\mathrm{V\,s^{-1}}$ and (3) exhibit an exponential dependence on the applied bias voltage $E_{\mathrm{bias}} = (E_{\mathrm{WE2}} - E_{\mathrm{WE1}})$. The insets A1 and A2 in Fig. 3a illustrate two examples of current vs. bias voltage plots of an early and of an advanced stage of the deposition on WE1. The nonlinear current increases several orders of magnitude from the nA to the μA range, and exhibits typical characteristics of electron tunneling across a square barrier. The Cu deposition on one of the electrodes reduces the gap width continuously (see also Sect. 3.3).

The third phase labelled IIIC is initialized by a sudden step in the current–time function followed by a sequence of additional steps which are separated by plateaus of variable length. The first current step marks the point of contact between WE1 and WE2 (indicated by the arrow in Fig. 3A). An atomically thin Cu contact is formed [18–28]. The corresponding conductance is estimated as $G_0 = 2e_0^2/h$, with e_0 being the elementary charge and h is Planck's constant. The height of the first discontinuous step varies between currents corresponding to 0.1 G_0 up to values close to 1 G_0, depending on the atomic configuration of the respective tunneling junction (see also Sect. 3.3). However, the experimentally observed plateau current is always linearly dependent on the applied bias potential [23]. Further deposition results in an increase in the diameter of the "nanowire" that bridges the two electrodes during which the conductance current (not the electrochemical Faraday current!) increases in a stepwise sequence until a continuous response is reached.

Finally, a current plateau evolves, which represents phase IIID. The growing wire exhibits macroscopic ohmic behavior (inset A3 in Fig. 3a). The limiting current is used to estimate the series resistance of the connecting leads, which contact the nanowires formed in phase IIIC.

After correction of the experimentally measured current for this contribution one obtains the junction conductance G. Figure 4a shows a series of normalized conductance traces G/G_0 for the repeated formation of nanocontacts by Cu deposition onto pre-fabricated Au nanoelectrodes. We observed single and multiple steps of G_0. The plot is restricted to the range $0 \leq G/G_0 \leq 12$ to reveal the initial stage of the contact formation.

Reversing the process by increasing the electrode potential of WE1 to more positive values leads to the dissolution of the Cu nanocontact. The latter was previously formed at more negative potentials. The conductance was monitored continuously during this "etching process" by measuring the current through the wire while maintaining a fixed bias voltage across it. The example plotted in Fig. 3b was recorded for $E_{\mathrm{WE1}} = -0.042\,\mathrm{V}$ and $E_{\mathrm{bias}} = (E_{\mathrm{WE2}} - E_{\mathrm{WE1}}) = 0.113\,\mathrm{V}$.

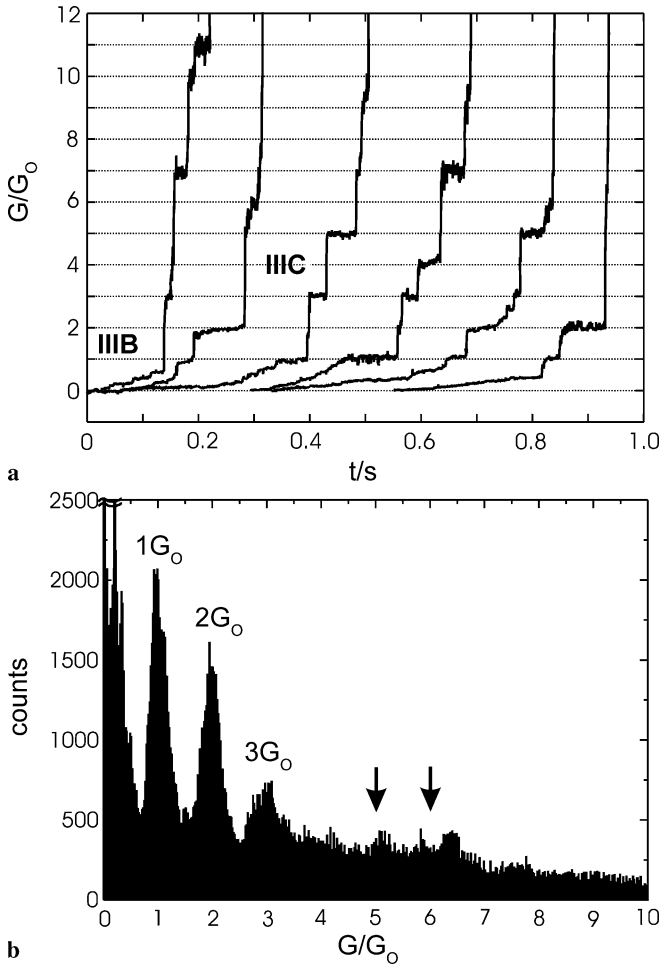

FIGURE 4 (**a**) Series of normalized conductance traces of the formation of Cu quantum wires at $E_{\mathrm{WE1}} = -0.163\,\mathrm{V}$ and $E_{\mathrm{WE2}} = -0.050\,\mathrm{V}$ in 0.1 M $H_2SO_4 + 1$ mM $CuSO_4$. The data shown are corrected for the series resistance of the connecting leads. (**b**) Conductance histogram for the repeated formation of Cu nanowires at $E_{\mathrm{WE1}} = -0.163\,\mathrm{V}$ and $E_{\mathrm{WE2}} = -0.050\,\mathrm{V}$. The *histogram* was constructed from over 100 conductance traces

The Cu "wire" narrows upon dissolution and finally breaks, accompanied by a stepwise decrease of the conductance current. The cross section and therefore the number of conductance channels decreases, which leads to a conductance quantization. The arrow in Fig. 3b indicates a single atomic contact. The corresponding plot G/G_0 vs. t is shown as inset B1 in Fig. 3b.

The rates of Cu dissolution and deposition can be tuned by the potentials E_{WE1} and E_{WE2} as well as by the preconditioning time in the Cu OPD respective UPD regions. Multiple dissolution and deposition cycles lead to a higher stability of the fabricated Cu nanocontacts. Similar findings were reported by Agrait et al. [15, 42] under UHV conditions and by Tao et al. [43] in electrolyte, who attributed this phenomenon to an improved crystallinity of the structures formed. Exploiting this phenomenon, and carefully adjusting the potentials of WE1 and WE2 we were able to form Cu nanocontacts, which were stable at a fixed conductance over several seconds without switching on an additional controlling feedback. An example is shown as insert B2 in Fig. 3b.

The current and the corresponding recalculated conductance traces (after correction for the series resistance of the contact leads) were analyzed quantitatively by constructing conductance histograms. A typical result is displayed in Fig. 4b, which was obtained for a series of more than 100 individual Cu deposition traces (cf.Fig. 4a) with $E_{\mathrm{WE1}} = -0.163\,\mathrm{V}$ and $E_{\mathrm{WE2}} = -0.050\,\mathrm{V}$. The first three peaks are well resolved at 1 G_0, 2 G_0 and 3 G_0. Less pronounced peaks were found at higher integer numbers of G_0 such as 5 G_0 and close to 6 G_0 (indicated by the arrow in Fig. 4b). Similar histograms were also obtained for Cu dissolution traces. The statistical analysis of the deposition and etching transients did not provide evidence for pronounced fractional conductance peaks below 5 G_0 for bias voltages smaller than 0.150 V. Because each abrupt conductance step corresponds to a rearrangement in the atomic configurations of the fabricated nanoelectrodes, we may conclude that 1 G_0, 2 G_0 and 3 G_0 represent particular stable atomic configurations of the Cu wires fabricated under our experimental conditions. Similar results were obtained in a STM configuration in UHV [44] and in electrolyte [18], as well as in experiments with vibrating macroscopic Cu wires under various ambient conditions [45]. We also like to comment on the large number of counts for $G < G_0$, which can be roughly represented by a single exponential decay. This feature marks the transition between direct tunneling and quantized conductance upon forming the first atomic contact. The comparison of the statistical analysis of our data for supported Cu nanocontacts with those reported for "free standing" contacts in a STM configuration [18, 44] reveals that the former exhibit a less abrupt transition between the two transport regimes. A detailed explanation is still lacking.

3.3 *Quantized tunneling current with nm-sized gaps*

Before the formation of an atomic contact between the growing wires, e.g. with the electrodes not yet touching, one observes an exponential increase of the current (phase IIIB). The width of the gap is continuously reduced by Cu deposition onto one of the electrodes. A particular example

is plotted in Fig. 5a. The experiment started with a gap stabilized at $E_{WE1} = -0.020\,V$ and $E_{WE2} = 0.080\,V$. The corresponding "initial" current $i_0 \sim 7\,nA$ is dominated by contributions from direct tunneling. Stepping the potentials E_{WE1} and E_{WE2} to $-0.120\,V$ and $-0.020\,V$ respectively, initializes the Cu deposition on WE1. The simultaneously recorded tunneling current increases exponentially, but in a stepwise regime. The step heights are not equally spaced, instead they appear to increase with the magnitude of the current. This behavior is different from the conductance quantization discussed in Sect. 3.2. The phenomenon of quantized tunneling was also reported in a STM configuration by Tao et al. [20]. The authors attributed their observation to the discrete nature of atoms and a series of structural relaxations between stable configurations upon deposition and dissolution. Additional contributions are expected from water molecules [46] and specifically adsorbed species [47], which are residing in the tunneling gap. The detailed microscopic structure of the tunneling junction is not yet known. Additional experimental and theoretical work is needed. However, empirical tuning of the electrode potentials of WE1 and WE2 allows the electrochemical annealing of the supported tunneling junction and the formation of gaps. Knowing the tunneling current and the bias voltage $E_{bias} = E_{WE2} - E_{WE1}$, the width of the gap Δs can be determined using the relation

$$i = E_{bias} G_0 \exp(-\kappa \Delta s)\,. \quad (1)$$

Assuming $\kappa = (10 \pm 1)\,nm^{-1}$, a typical value of the decay constant in aqueous electrolyte [47], and a linear proportionality between the gap width Δs and the deposition t, we obtain a distance scale of the gap width (cf. inset in Fig. 5). With this knowledge and a careful adjustment of deposition and monitoring potentials, temporarily stable molecular sized Cu gaps with distances between 0.4 nm up to 2.0 nm could be fabricated. Figure 5b displays, as an example, a stabilized Cu|Cu gap at $i_0 = 7\,nA$ ($\Delta s \sim 0.7\,nm$) for $E_{WE1} = -0.020\,V$ and $E_{WE2} = 0.080\,V$. However, due to the high surface mobility of Cu atoms and the absence of an activated feedback circuit, the stability of these gaps was typically ≤ 1 s. This stability is not yet sufficient. The combination of the developed electrochemical approach with an appropriate active feedback circuit appears to be a promising route to prepare nanoscale gaps as templates for further applications.

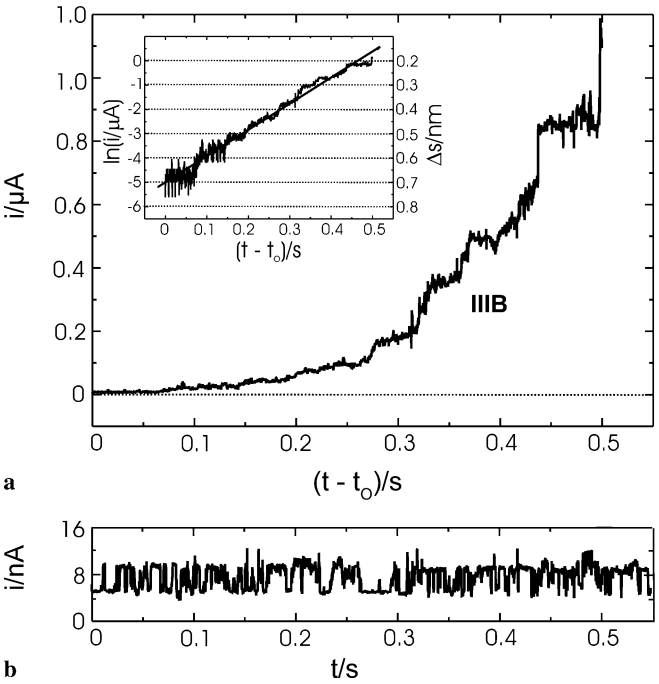

FIGURE 5 (**a**) Stepwise change of the tunneling current (phase IIIB) for Cu deposition at $E_{WE1} = -0.120\,V$ and $E_{WE2} = -0.020\,V$ in 0.1 M $H_2SO_4 + 1$ mM $CuSO_4$. The nucleation was initialized at $E_{WE1} = -0.250\,V$, and at $t = t_0$ the potential was stepped to $E_{WE1} = -0.163\,V$. The *inset* shows the tunneling current in logarithmic scale and the corresponding gap width. The latter was obtained assuming that zero gap width occurs at quantum-point contact. (**b**) Temporarily stabilized Cu|Cu gap at $i_0 = 7\,nA$ ($\Delta s \sim 0.7\,nm$) for $E_{WE1} = -0.020\,V$ and $E_{WE2} = 0.080\,V$

4 Summary and conclusions

1. A dedicated low-current four-electrode bipotentiostat equipped with temperature-stabilized logarithmic current-to-voltage converters, and with capabilities for a wide range of analog and digitally generated excitation signals, was developed for controlling the electrochemical fabrication process and for monitoring the electrical characteristics of the created nanostructures.
2. Sustainable Cu nanocontacts were prepared by potentiostatic electrodeposition of Cu onto Au wires supported on an insulating solid substrate. The potentials E_{WE1} and E_{WE2} were chosen such that the deposition proceeded preferentially on one of the gold electrodes (WE1), while the Faraday current on the other electrode (WE2) was negligible. The tunneling respective conductance characteristics of the junction were continuously monitored. Two approaches were chosen: (method 1) – recording of current time traces at a small bias voltage; (method 2) – measuring the current while ramping the bias voltage to large values with a scan rate of $20\,V\,s^{-1}$. The latter is a specific characteristic of the chosen asymmetric electrodeposition strategy, which allows keeping E_{WE1} constant while ramping E_{WE2} without modifying the Cu deposition on WE1. Nanoscale gaps exhibit an exponential i vs. E_{bias} characteristic. The current through nanocontacts is linearly dependent on the applied bias voltage.
3. The statistical analysis of conductance histograms, which were constructed from current time traces (method 1), revealed the preferential stability of nanocontacts with integer values of G_0 with a clear preference for 1 G_0, 2 G_0 and 3 G_0. These conductance values represent particular stable atomic configurations of the Cu nanocontacts fabricated under our experimental conditions. Without applying an external feedback signal we could manually stabilize these junctions by carefully adjusting the electrode potentials up to 2 s. No evidence was found for the occurrence of fractional conductance peaks below 5 G_0.
However, in comparison to "free standing" nanocontacts fabricated in a vertical STM configuration, we observed a large number of counts for $G < G_0$. This finding might indicate the existence of temporarily stable tunneling configurations.

4. Nanocontacts were broken by Cu dissolution (or "etching"), which could be reversibly triggered by tuning the electrode potentials E_{WE1} and E_{WE2} to values positive of the OPD deposition, region III. We observed similar conductance quantization as for the formation of the nanocontacts.
5. An exponential, but step-like increase of the current is observed before the formation of an atomic contact between the growing wires. This quantized tunneling current is attributed to the discrete nature of Cu atoms and respective molecular (water) ionic adsorbates in the junction. The width of the gap was estimated based on the measured current–time characteristics assuming a tunneling coefficient $\kappa \sim 10\,\mathrm{nm}^{-1}$ in aqueous electrolyte and zero gap width at quantum point contact. We could stabilize molecular sized gaps typically for $t \leq 1$ s without applying an external feedback signal.
6. Despite the still existing limitations in the long-term stability of nanocontacts and molecular-sized gaps, we have established in this research the principles for fabricating stable nanogaps in an electrochemical environment. Introduction of an automatic feedback circuit for tuning the interplay between deposition and dissolution, and extending the work to systems with a much larger potential range of ideal polarizability, such as gold or palladium, offers a high potential for fabricating nanogaps and -contacts, which are more stable under in situ as well as ex situ conditions. They may act as templates for further functionalization with nanoscale objects, such as tailored molecules, clusters or nanotubes.

ACKNOWLEDGEMENTS This work was supported by the Volkswagen Foundation, the HGF Project "Molecular Switches", IFMIT and the Research Center Jülich. G.M. acknowledges the support of the German Academic Exchange Agency for a fellowship and the Hungarian Science Research Fund (OTKA T 42452). We also thank A. van der Hart, H. Haselier and M. Wingens for the skillful preparation of the e-beam structures.

REFERENCES

1 J.D. Meindel, Q. Chen, J.A. Davis, Science **293**, 2044 (2001)
2 R.L. McCreery, Chem. Mater. **16**, 4477 (2004)
3 B.A. Mantooth, P.S. Weiss, Proc. IEEE **91**, 1785 (2003)
4 U. Banin, Y. Cao, D. Katz, O. Millo, Nature **400**, 542 (1999)
5 D.L. Klein, R. Roth, A.K.L. Lim, A.P. Alivisatos, P. McEuen, Nature **389**, 699 (1997)
6 Z. Chen, J. Appenzeller, Y.M. Lin, J. Sippel-Oakley, A.G. Rinzler, J. Tang, S.J. Wind, P.M. Solomon, P. Avouris, Science **311**, 1735 (2006)
7 Y. Xia, P. Yang, Y. Sun, Y. Wu, B. Mayers, B. Gates, Y. Yin, F. Kim, H. Yan, Adv. Mater. **15**, 353 (2003)
8 E.C. Walter, K. Ng, M.P. Zach, R.M. Penner, F. Favier, Microelectron. Eng. **61–62**, 555 (2002)
9 A. Aviram, M. Ratner, V. Mujica (Eds.), *Molecular Electronics II* (Ann. NY Acad. Sci., New York, 2002)
10 M.A. Guillorn, D.W. Carr, R.C. Tibeno, E. Greenbaum, M.L. Simpson, J. Vac. Sci. Technol. B **18**, 1177 (2000)
11 A. Bezryadin, C. Dekker, G. Schmid, Appl. Phys. Lett. **71**, 1273 (1997)
12 C. Zhou, M.R. Deshpande, M.A. Reed, H.L. Jones, J.M. Tour, Appl. Phys. Lett. **71**, 611 (1997)
13 R. Sordan, M. Burghard, K. Kern, Appl. Phys. Lett. **79**, 2073 (2001)
14 C.J. Muller, J.M. van Ruitenbeek, L.J. de Jongh, Physica C **191**, 485 (1997)
15 N. Agrait, A. Levi-Yeyati, J.M. van Ruitenbeek, Phys. Rep. **377**, 81 (2003)
16 J.K. Gimzewski, R. Moller, Phys. Rev. B **36**, 1284 (1987)
17 H. Park, P.K.L. Lim, A.P. Alivisatos, J. Park, P.L. McEuen, Appl. Phys. Lett. **75**, 301 (1999)
18 C.Z. Li, N.J. Tao, Appl. Phys. Lett. **72**, 894 (1998)
19 A.F. Morpurgo, C.M. Marcus, D.B. Robinson, Appl. Phys. Lett. **74**, 2084 (1999)
20 C.Z. Li, H.X. He, N.J. Tao, Appl. Phys. Lett. **77**, 3995 (2000)
21 J. Li, Y. Yamada, K. Murakoshi, Y. Nakato, Chem. Commun. 2170 (2001)
22 Y.V. Kervennic, H.S.J. van der Zant, A.F. Morpurgo, L. Gurevich, L.P. Kouvenoven, Appl. Phys. Lett. **80**, 321 (2002)
23 S. Boussaad, N.J. Tao, Appl. Phys. Lett. **80**, 2398 (2002)
24 J. Li, T. Kanzaki, K. Murakoshi, Y. Nakato, Appl. Phys. Lett. **81**, 123 (2002)
25 Y. Kashimura, H. Nakashima, K. Furukawa, K. Torimitsu, Thin Solid Films **438**, 317 (2003)
26 M.M. Deshmukh, A.L. Prieto, Q. Gu, H. Park, Nano Lett. **3**, 1383 (2003)
27 L.H. Yu, D. Natelson, Appl. Phys. Lett. **82**, 2332 (2003)
28 F. Elhoussine, A. Encinas, S. Matefi-Tempfli, L. Piraux, J. Appl. Phys. **93**, 8567 (2003)
29 Y.V. Kervennic, D. Vanmaekelbergh, L.P. Kouwenhoven, H.S.J. van der Zant, Appl. Phys. Lett. **83**, 3782 (2003)
30 F.Q. Xie, L. Nittler, C. Obermair, T. Schimmel, Phys. Rev. Lett. **93**, 128 303-1 (2004)
31 J. Xiang, B. Liu, S.T. Wu, B. Ren, F.Z. Yang, B.W. Mao, Y.L. Chow, Z.Q. Tian, Angew. Chem. Int. Edit. **44**, 1265 (2005)
32 Q. Qing, F. Chen, P. Li, W. Tang, Z. Wu, Z. Liu, Angew. Chem. Int. Edit. **44**, 7771 (2005)
33 U. Landman, Proc. Nat. Acad. Sci. **102**, 6671 (2005)
34 B. Xu, H. He, S. Boussaad, N.J. Tao, Electrochim. Acta **48**, 3085 (2003)
35 N.J. Tao, Nature Nanotechnol. **1**, 173 (2006)
36 S. Kronholz, S. Karthäuser, A. van der Hart, T. Wandlowski, R. Waser, Microelectron. J. **37**, 591 (2006)
37 G. Meszaros, T. Wandlowski, Rev. Sci. Instrum. (2007), in preparation
38 T. Wandlowski, K. Ataka, S. Pronkin, D. Diesing, Electrochim. Acta **49**, 1233 (2004)
39 M.A. Schneeweiss, D.M. Kolb, Phys. Stat. Solidi A **173**, 51 (1999)
40 T. Wandlowski, unpublished
41 A.J. Bard, L.R. Faulkner, *Electrochemical Methods – Fundamentals and Applications* (Wiley, New Jersey, 2001)
42 G. Rubio, N. Agrait, S. Viera, Phys. Rev. Lett. **76**, 2302 (1996)
43 C.Z. Li, A. Bogozi, W. Huang, N.J. Tao, Nanotechnology **10**, 221 (1999)
44 L. Olesen, E. Lengsgaard, I. Stensgaard, F. Besenbacher, J. Schiotz, R. Stolze, K.W. Jacobsen, J.K. Norskov, Phys. Rev. Lett. **72**, 2251 (1994)
45 J.L. Costa-Krämer, N. Garcia, P. Garcia-Mochales, P.A. Serena, Surf. Sci. **342**, L1144 (1995)
46 S. Boussaad, B.Q. Xu, L.A. Nagahara, I. Amlani, W. Schmickler, R. Tsui, N.J. Tao, J. Chem. Phys. **118**, 889 (2003)
47 G. Nagy, T. Wandlowski, Langmuir **19**, 10 271 (2003)